ELSEVIER

Journal of Fluids and Structures 25 (2009) 60–79

JOURNAL OF FLUIDS AND STRUCTURES

www.elsevier.com/locate/jfs

Unsteady phenomena of an oscillating turbulent jet flow inside a cavity: Effect of aspect ratio

A. Mataoui[a,*], R. Schiestel[b]

[a]*Laboratoire de Mécanique des Fluides, Faculté de Physique, Université des sciences et de la technologie Houari Boumediene – UST.H.B, B.P. 32, Bab Ezzouar, 16111 Al Alia, Alger, Algérie*

[b]*Institut de Recherche sur les Phénomènes Hors Equilibre, I.R.P.H.E., U.M.R. 6594 CNRS/Universités d'Aix-Marseille I & II, 49, rue Frédéric Joliot Curie, B.P. 146, 13384 MARSEILLE Cedex 13, France*

Received 18 June 2007; accepted 31 March 2008
Available online 15 July 2008

Abstract

Self-sustained oscillatory phenomena in confined flow may occur when a turbulent plane jet is discharging into a rectangular cavity. An experimental set-up was developed and the flow analysis has been made using mainly hot-wire measurements, which were complemented by visualisation data. Previous studies confirmed that periodic oscillations may occur, depending on the location of the jet exit nozzle inside the cavity, and also the distance between the side-walls. The present study deals with the symmetrical interaction between a turbulent plane jet and a rectangular cavity and the influence of the geometrical characteristics of the cavity on the oscillatory motion. The size and aspect ratio of the cavity were varied together with the jet width compared to that of the cavity. The study is carried out both numerically and experimentally. The numerical method solves the unsteady Reynolds averaged Navier–Stokes equations (URANS) together with the continuity equation for an incompressible fluid. The closure of the flow equations system is achieved using a two-scale energy-flux model at high Reynolds number in the core flow coupled with a wall function treatment in the vicinity of the wall boundaries. The fundamental frequency of the oscillatory flow was found to be practically independent of the cavity length. Moreover, the oscillations are attenuated as the cavity width increases, until they disappear for a critical value of the cavity width. Contour maps of the instantaneous flow field are drawn to show the flow pattern evolution at the main phases of oscillation. They are given for several aspect ratios of the cavity, keeping constant values for the cavity width and the jet thickness. The proposed approach may help to investigate further the oscillation mechanisms and the entrainment process occurring in pressure driven jet–cavity interactions.

Keywords: Unsteady flow; Plane jet; Turbulence; Cavity; Phase shift; Oscillatory; Flow; Visualisation

1. Introduction

The case of a turbulent plane jet flowing into a rectangular cavity with a closed end will be considered. It is a flow configuration in which a self-oscillatory behaviour may occur under some geometrical conditions. Self-excited

*Corresponding author. Tel.: +213 772 72 38 45; fax: +213 21 24 73 44.
E-mail address: mataoui_amina@yahoo.fr (A. Mataoui).

0889-9746/$ - see front matter © 2008 Elsevier Ltd. All rights reserved.
doi:10.1016/j.jfluidstructs.2008.03.010

oscillations are then produced by the periodic deflection of the jet axis due to pressure effects or Coanda effect. The Coanda effect which was approximately discovered half a century ago [see Bourque and Newman (1960)], appears to be the fundamental physical phenomenon that causes the jet to oscillate in the cavity, provided some limiting conditions in the ratio of the impingement length of the jet to the width of the cavity are satisfied independently of Reynolds number. These oscillations are mainly sustained by two distinguishable swirling eddies at each side of the jet within the cavity. These eddies produced and modulated by the periodic jet deflections can be detected by the occurrence of negative pressure levels. These negative pressures are induced by the reverse flow, which is blocked by a vortex appearing at the exit, located at the free open side (Coanda effect).

These oscillations correspond to natural unsteadiness generated by a hydrodynamic instability developing in a jet flowing between two counter-rotating eddies. Such self-sustained oscillations are driven by the jet deflection mechanism produced by the pressure variations (Coanda effect).

Similar phenomena may also be related to other mechanisms: to the shear layer instability in a shallow cavity (Rockwell and Naudascher, 1979; Pereira and Sousa, 1995; Sarohia, 1977); to the separating flow over a back step or a cavity (Sinha et al., 1982); to the blind cavity effect (Molloy, 1969) and the cross-flow instability (Lawson and Davidson, 1999).

Oscillations may occur in both laminar flow regime [(Maurel et al. (1996); see also Battaglia et al. (1998)] and turbulent flow regime (Guo et al., 2001; Gebert et al., 1998) at different geometrical parameters and boundary conditions.

In the present case, the oscillations disappear when the jet exit is close to one of the side-walls of the cavity, thus generating a longitudinal quasi-stationary interaction with the nearest side-wall to the exit of the jet (Mataoui et al., 2001). When the jet exit nozzle is sufficiently close to the cavity bottom, a quasi-steady flow is also produced by the perpendicular impingement of the jet on the bottom wall (Bernard et al., 2000; Mataoui et al., 2001).

For a turbulent plane jet flowing into a rectangular cavity as considered in the present work, several flow regimes appear depending on the location of the jet exit inside the cavity. Three different regimes were observed (Mataoui et al., 2003): a periodic oscillatory flow, a steady flow with no oscillation, and an irregular flow regime with chaotic behaviour.

Generally, fluctuations occur when the jet exit is sufficiently far from the two side-walls and from the cavity bottom. Particularly, when the jet exit is located symmetrically and at a certain distance from the bottom of the cavity, the flow is generally fully periodic. In the symmetrical interaction case, several researchers have then observed the flapping phenomenon of the jet between the upper and the lower side planes of a cavity. We can mention in particular: Shakouchi (1981), Ogab (1985), Maurel (1994), Lawson (2001) and Lawson et al. (2005), Gloerfelt and Lafon (2005) and Kolšek et al. (2007). A minor asymmetry in the jet exit location, departing slightly from the middle plane of the cavity, may also contribute in sustaining these oscillations (Mataoui et al., 2001).

Oscillations may cease depending on several geometrical parameters of the cavity, such as shallow aspect ratios and large nozzle diameters at the jet exit (Lawson et al., 2005; Shakouchi, 1981; Shakouchi et al., 1982). In the present study, we consider the influence of various geometrical parameters in the symmetrical interaction of a turbulent jet in a rectangular cavity. The oscillations of a jet inside a cavity have been the subject of several research works since the pioneering papers of Shakouchi (1981), Shakouchi and Kuzuhara (1982) and Ogab (1985). Then, other researchers have contributed to develop the study of this phenomenon, among them we can mention Maurel (1994), Maurel et al. (1996), Villermaux and Hopfinger (1994), Uzol and Camci (2002), Lawson (2001), Lawson et al. (2005), Mataoui et al. (2001, 2003), Gevici et al., 2003 and Denisikhina et al. (2005) who achieved a valuable numerical work using URANS and LES. We also mention again the work of Battaglia et al. (1998) dealing with the interaction of a jet in a channel.

From the practical point of view, jet oscillations are currently involved in various applications in fluid mechanics processes, as follows. (i) In recent years, there have been several investigations devoted to the development of fluidic flow-meters for domestic or industrial uses (Hebrard et al., 1979; Shakouchi, 1989; Maurel, 1994; Pacheu et al., 2000). (ii) Problem of mixing in fluid flow, combustion, and cooling or heating by means of forced convection, with a number of interesting industrial applications in heat transfer processes. (iii) Air-conditioning devices, fluid renewal inside of a cavity and the ventilation of the underground galleries and mines are typical potential applications.

2. The experimental set-up

A perspective view of the experimental set-up is reported in Fig. 1. The jet velocity U_0 at the nozzle exit can be varied from 2 to 20 m/s, thus giving a Reynolds number, based on the nozzle height e (= 1.0 cm), ranging from 1333 to 13,330. The cavity is a parallelepipedic box made of transparent plexiglas in order to easily visualize the flow resulting from the jet–cavity interaction.

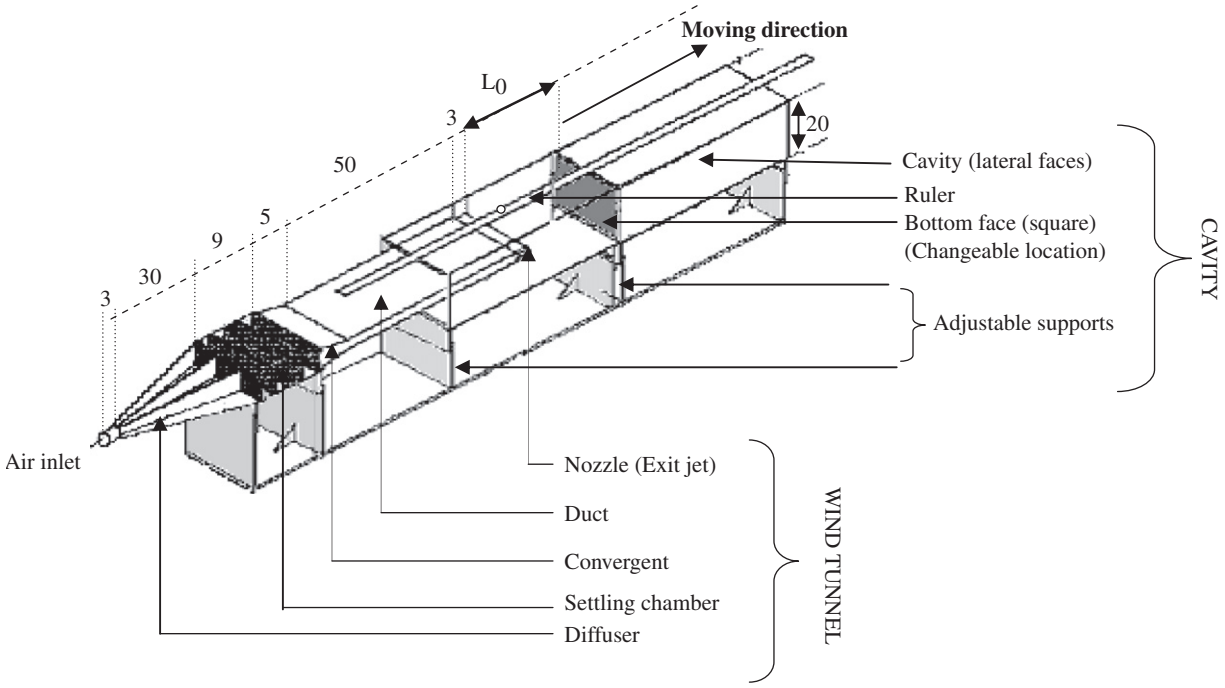

Fig. 1. Experimental set-up (dimensions given in cm).

The main parts of the experimental set-up are as follows:

(a) A wind tunnel which generates a plane jet with low turbulence intensity; the height and the width of the nozzle outlet remain constant in all the measurements (Fig. 1).

(b) The rectangular cavity with the jet exit nozzle located inside and closed by an end wall. A ruler fitted with an opening to introduce the probes support inside the cavity is disposed on the upper wall of the cavity. The nozzle exit can be displaced inside the cavity and located at the desired position as shown in Fig. 1. In the present study, the cavity width and height are kept constant; the cavity lateral spanwise dimension is 20 cm, equivalent to that of the jet nozzle transverse width, while the length of the cavity can be adjusted in order to investigate the influence of the bottom wall location on the flow characteristics.
The wind tunnel duct and the nozzle exit are located symmetrically in front of the cavity and they can be displaced both horizontally and vertically within the cavity by adjustable supports.
Hot-wire measurements were carried out with a Dantec multi-channel constant temperature anemometer (CTA system 56C00) for instantaneous velocity measurements. Calibration of the probes was produced with a DISA unit 55D45. The single hot-wire probe DISA 55P11 probes made of a 5 μm diameter platinum-plated tungsten wire. A traversing mechanism was built to move the probe along the streamwise direction and in the vertical direction. A slot was managed in the sliding ruler to allow the probe support to reach any location inside of the cavity. In the case of instantaneous quantities, the CTA hot-wire anemometry is preferred to the laser Doppler anemometry (LDA) as discussed by Bruun (1995) regarding the quality of the response of the wire. The geometrical size of the cavity is L_0 in length and H_0 in height, or in dimensionless form:

$$L_0^* = \frac{L_0}{e} \quad \text{and} \quad H_0^* = \frac{H_0}{e}.$$

(c) The velocity signal analysis devices.

(d) A white smoke generator (CFT Taylor) used to visualize the flow structure. This generator produces a white smoke consisting of very small droplets of vegetable oil mixed with compressed carbon dioxide. The smoke is injected upstream at the entrance of the duct in order to get a white homogeneous smoke at the jet exit.

(e) A light projector. The light beam was directed through a vertical transparent area located in the median plane of the cavity bottom. Animated photograph series were produced using a stroboscopic camera at a pace of 2 pictures per second.

3. Turbulence modelling

A two-scale energy-flux model is adopted in this study. Multiple-scale modelling was previously proposed by Schiestel (1987) after the work of Launder and Schiestel (1978), Hanjalic et al. (1980) and Schiestel (1983). The rationale of this choice is related to the unsteadiness of the present turbulent flow, in which large space and time variations may lead to departures from equilibrium (Mataoui et al., 2001).

3.1. Governing equations of motion

The RANS equations for a two-dimensional unsteady, incompressible flow in Cartesian coordinates are deduced from the mass and momentum balance equations as follows:

$$\frac{\partial U_i}{\partial X_i} = 0, \tag{1}$$

$$\frac{\partial U_i}{\partial t} + U_j \frac{\partial U_i}{\partial X_j} = -\frac{\partial}{\partial X_i}\left(\frac{P}{\rho}\right) + \frac{\partial}{\partial X_j}\left(\nu \frac{\partial U_i}{\partial X_j} - \overline{u_i u_j}\right). \tag{2}$$

Eq. (2) contains the Reynolds stress terms for which a closure model must be introduced.

3.2. Two-scale turbulence closure

This two-scale energy-flux model is based on the concept of eddy turbulent viscosity. As mentioned earlier, the present flow configuration, which implies separation and reattachment phenomena together with strong variations in space and time, may induce departures from spectral equilibrium. Therefore, as in Mataoui et al. (2001), we have implemented the multiscale approach for turbulence modelling. The fundamental principles of this formalism are extensively discussed in Schiestel (1987, 2006). Multiple-scale modelling takes into account the fact that turbulence is characterized by a wide spectrum of fluctuations. Besides, turbulent interactions are associated with different parts of this evolving spectrum.

The energy-flux model is based on a simplified split spectrum scheme (Schiestel, 1983, 1987) based on the portioning of the turbulence energy spectrum into three zones (Fig. 2) delimited by their corresponding wavenumbers κ_P and κ_T. The $[0, \kappa_P]$ interval corresponds to the wavenumber region in which the main shear production is active, while the $[\kappa_P, \kappa_T]$ wavenumber interval corresponds to the energy cascade transfer zone and then the viscous dissipation zone $[\kappa_T, \infty]$ follows. Energy is transferred out of the first region (production zone) at a rate κ_P and injected into the transfer zone. Then the energy leaving the transfer zone at a rate κ_T is transferred towards the dissipation zone in which it is dissipated at a rate ε. The hypothesis that the dissipation zone contains no appreciable energy allows to suppose $\varepsilon = \varepsilon_T$.

Therefore, the two dimensionless parameters k_P/k_T and $\varepsilon_P/\varepsilon_T$ can be viewed as non-equilibrium indicators. The former characterizes the shape of the energy spectrum, while the latter represents the level of the spectral flux imbalance.

The multiple-scale model is a simple scheme suitable to mimic the cascade delays in the spectral pipeline. The energy distribution is obtained through the solution of the transport equations for partial energies and fluxes in each zone of the spectrum. The splitting allows the energy flux ε_P transferred out of the production zone to be directly influenced by the shear production source term, while the energy flux ε_T evolve with some time delay.

The partial kinetic energies are determined from the following transport equations:

$$\frac{\mathrm{d}k_P}{\mathrm{d}t} = \nu_t (U_{i,m} + U_{m,i}) U_{i,m} + \left[\left(\nu + \frac{\nu_t}{\sigma_{kP}}\right) k_{,m}\right]_{,m} - \varepsilon_P, \tag{3}$$

$$\frac{\mathrm{d}k_T}{\mathrm{d}t} = \varepsilon_P + \left[\left(\nu + \frac{\nu_t}{\sigma_{kT}}\right) k_{,m}\right]_{,m} - \varepsilon_T. \tag{4}$$

The total turbulent kinetic energy must be equal to the sum of the two partial kinetic energies:

$$k = k_P + k_T.$$

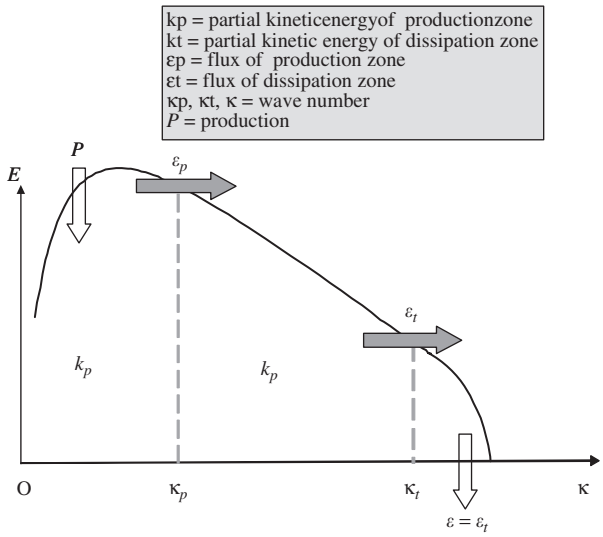

Fig. 2. Scheme of partition energy spectrum.

The spectral fluxes are also obtained from separate transport equations:

$$\frac{\mathrm{d}\varepsilon_P}{\mathrm{d}t} = C_{1P}\frac{\varepsilon_P}{k_P}v_t(U_{i,m}+U_{m,i})U_{i,m} + \left[\left(v+\frac{v_t}{\sigma_{\varepsilon P}}\right)\varepsilon_{P,m}\right]_{,m} - C_{2P}\frac{\varepsilon_P^2}{k_P}, \tag{5}$$

$$\frac{\mathrm{d}\varepsilon_T}{\mathrm{d}t} = C_{1T}\frac{\varepsilon_P\varepsilon_T}{k_T} + \left[\left(v+\frac{v_t}{\sigma_{\varepsilon T}}\right)\varepsilon_{T,m}\right]_{,m} - C_{2T}\frac{\varepsilon_T^2}{k_T}, \tag{6}$$

$$\varepsilon = \varepsilon_T, \tag{7}$$

where C_{1P}, C_{2P}, C_{1T} and C_{2T} can be considered as numerical constants or as functions of the spectrum shape parameters defined by $\xi = k_P/k_T$ and $\theta = \varepsilon_P/\varepsilon_T$. As a first approximation we will assume constant numerical values for these coefficients. In equilibrium situations, $\varepsilon_P = \varepsilon_T = \varepsilon$ and the model behaves like a standard $k-\varepsilon$ model. The numerical values of the modelling constants in the transport equations are:

$$C_{1P} = 1.65; \quad C_{2P} = 1.92; \quad C_{1t} = 1.75; \quad C_{2t} = 1.82.$$

As a result, it can be shown easily that in equilibrium conditions, the dimensionless parameters take on the numerical values $\xi = 3$ and $\theta = 1$. The turbulent eddy viscosity v_t is given by the equation $v_t = c_\mu k^2/\varepsilon_P$.

The question can be raised whether URANS methods are an adequate framework for tackling the problem. We can point out that the basic interaction mechanism that prevails in the present experiment is mainly the pressure–velocity coupling of the jet in a confined environment, this is the driving force of the fluctuations and the flapping phenomenon. Once the oscillation mechanism has been initiated, the mean part of the flow becomes unsteady and this mechanism could be effective in laminar flows as well. This is why URANS modelling seems appropriate; the URANS model describes the (relatively slow) unsteady evolution of the mean part of the flow, while standard modelling is used for the true turbulence field. The physical mechanisms analysed in the Villermaux and Hopfinger (1994) paper are not exactly the same, they are initiated by the preferred mode of the jet instability, and probably in such a case large eddy simulation methods would be necessary.

3.3. Near-wall modelling

Considering that the driving forces in the present unsteady phenomena are mainly due to pressure effects, there is no need for a detailed solution of the viscous sublayer in the wall treatment. Therefore, we shall use high Reynolds number closure in the core flow coupled with a standard wall function technique (Launder and Spalding, 1974; Patankar, 1980) that bridges the no-slip wall condition to the fully turbulent core flow using logarithmic profiles. This simplified method proved to be adequate for this problem (Mataoui et al., 2001).

Consequently, the standard logarithmic law of the wall defined by Launder and Spalding (1974) was imposed for all the walls present in the configuration (the cavity walls and duct side-walls) as a boundary condition in its generalised form in which N denotes the grid point located nearest to the wall:

$$U^+ = \frac{U}{U_*} = \frac{1}{\kappa}\,\mathrm{Log}\,Ey_N^+ \quad \text{for } y_N^+ > 11.0\,(\kappa = 0.41, E = 9.0); \tag{8}$$

$$U^+ = y^+ \quad \text{for } y_N^+ < 11.0. \tag{9}$$

This latter equation for $y_N^+ < 11.0$ is only used at some exceptional points.

The skin friction and normalized distance to the wall are defined as follows:

$$U_* = \frac{\tau_w}{\rho c_\mu^{1/4} k_N^{1/2}} \quad \text{and} \quad y^+ = \frac{y c_\mu^{1/4} k_N^{1/2}}{\nu}.$$

Because of this simple practical choice, the detailed structure of the flow in the vicinity of the wall cannot be accurately obtained [see Craft et al. (1993), Cooper et al. (1993), Yap (1987)]. But this is not the aim of the present study and considering that the flow is mainly driven by pressure forces, the influence of the logarithmic boundary conditions at the walls will remain very limited.

4. Numerical method

A finite volume method was used. It requires the integration of the mean and turbulent field transport equations over the discretization cells. The numerical solution of that system of equations is obtained with an elliptic solver which is based on the tridiagonal algorithm with sub-iterations.

Staggered meshes for the velocity components were used in order to prevent the development of checkerboard instabilities throughout the pressure field. The well-known SIMPLE algorithm (see Patankar, 1980) was applied for the pressure–velocity coupling. As usual, the source terms of the turbulence equations were linearized to ensure the solution stability, whilst the nonlinearities were solved through internal iterations. Such a technique is computationally inexpensive, as it requires reduced storage capacities.

The present flow shows a considerable variation in the velocity vector direction near the impact location at the wall; therefore, for this reason, a double sweep with the tridiagonal algorithm was applied along the vertical and horizontal directions to accelerate convergence.

All the boundary conditions are summarised in Fig. 3, as follows.

(a) The inlet boundary conditions (at the nozzle) are assumed to be constant for all the variables.
(b) The near-wall treatment is based on the universal logarithmic law of the turbulent boundary layer.
(c) At the open boundaries, two cases may occur depending if the fluid is leaving out or entering the cavity. The boundary conditions for the different variables Φ representing (V, k, k_P, k_T, ε, ε_P , ε_T) are detailed hereafter: (i) in the first case, with the fluid entering the cavity (aspiration of fluid from outside: $U<0$) the values Φ_{ext} are imposed: $\Phi = \Phi_{\mathrm{ext}}$; (ii) in the second case, with the fluid leaving the cavity ($U>0$), free Neumann conditions are imposed, $\partial\Phi/\partial x = 0$. In both cases, the pressure at the free boundary is imposed and the U velocity component is deduced from the continuity equation.

The convection–diffusion scheme is the power law approximation (Patankar, 1980). First of all, grid independence tests have been made in a steady case for several values of grid size. Generally, a grid size of $NX = 100$ and $NY = 80$ for the basic reference case ($L_0^* = 50$, $H_0^* = 20$) produces satisfactory accuracy in the results. Indeed, for an increased grid size of $NX = 120$ and $NY = 100$, the observed variation in the calculated quantities remains less than 2%. In the elongated cavity ($L_0^* = 100$, $H_0^* = 20$) the grid was composed of 150×80 points. A grid refinement upstream and downstream the nozzle exit was applied so that the entrainment was accurately described. The meshes were also refined vertically near the jet exit (in order to have sufficient accuracy near the edge of the nozzle). A small refinement of the grid was also introduced near the cavity walls and the duct walls because of strong gradients.

In the unsteady calculations, the time scheme is only first order, but small time steps have been used. It must be recalled also that the frequency of oscillation of the flow is relatively slow, and very small compared to the characteristic frequencies of turbulence. Tests have also been done to determine the appropriate choice of the time step. The Courant number (defined by $C = \max(U\delta t/\delta x, V\delta t/\delta y)$) in the unsteady calculations is about unity in most of the flow field.

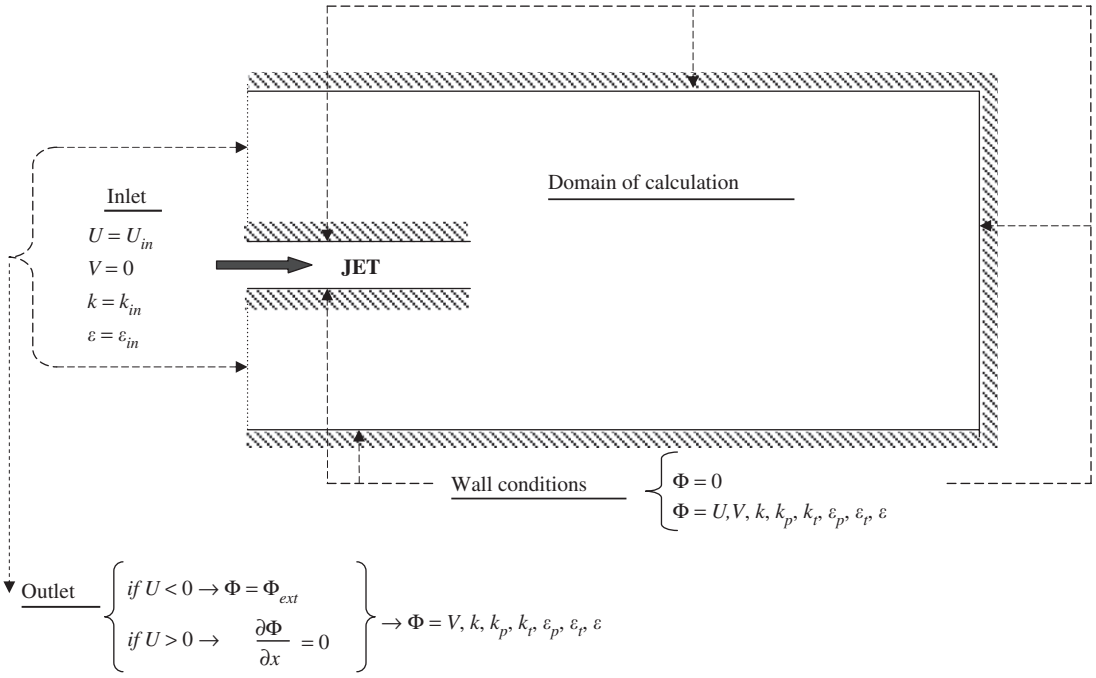

Fig. 3. Boundary conditions.

Indeed, due to the use of an implicit time scheme, the CFL condition is not required. About 50 or more time steps are used to describe one period of evolution. The calculations of three or four successive periods are sufficient to get truly periodic results.

5. Results and discussion

Depending on the values of the geometrical parameters, the flow produced by the interaction between the jet and the cavity exhibits different possible behaviours. These various observed situations are reported hereafter:

1st case: The jet oscillates periodically.

2nd case: A stable oblique or perpendicular interaction occurs respectively on the upper wall or the lower wall or even the bottom of the cavity.

3rd case: An irregular interaction, with chaotic unsteadiness which characterizes an intermediate situation between the two previous cases.

5.1. Parameters of the problem

The dynamical and geometrical parameters considered in the present study are defined by the sketch in Fig. 4. The dynamical parameter involved in the present study is the Reynolds number based on the jet exit velocity U_0, the nozzle height ($e = 10^{-2}$ m) and kinematic viscosity v of the fluid (air): $\mathrm{Re} = U_0 e/v$.

The oscillation frequency in the case of the oscillatory flow is characterized by the Strouhal number based on the characteristics of the jet at the exit (U_0 and e) and the oscillation frequency f: $\mathrm{St} = fe/U_0$.

The current measurement point M is determined by its coordinates $M(L, H)$ reported in Fig. 4, and in dimensionless form ($L^* = L/e$, $H^* = H/e$). The jet exit location is (L_0, $H_0/2$).

Additionally, two other dynamical quantities are considered: the mass flow rate at the outlet Q_{upper} and Q_{lower}, respectively, through the upper and the lower exit sections of the cavity and the flow rate at the jet exit Q_0 which verifies the conservation condition:

$$Q_{\mathrm{upper}} + Q_{\mathrm{lower}} = -Q_0.$$

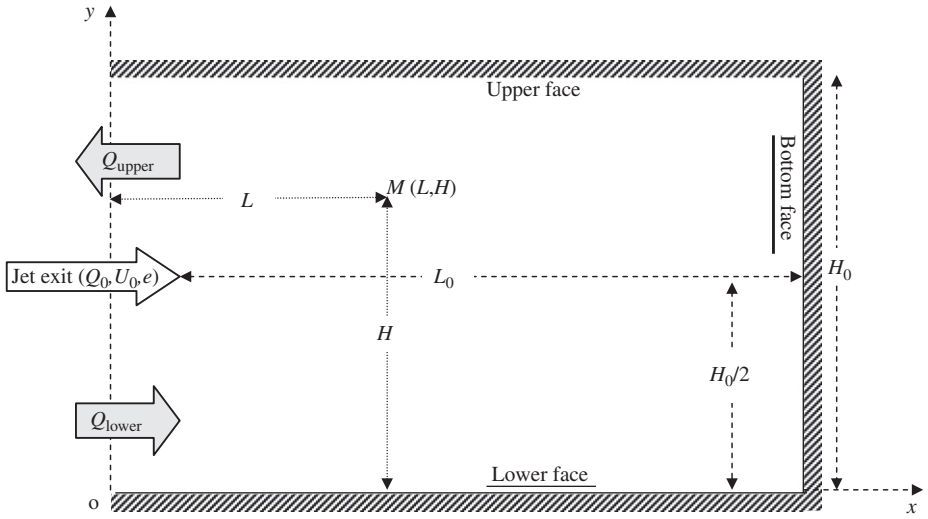

Fig. 4. The flow control parameters.

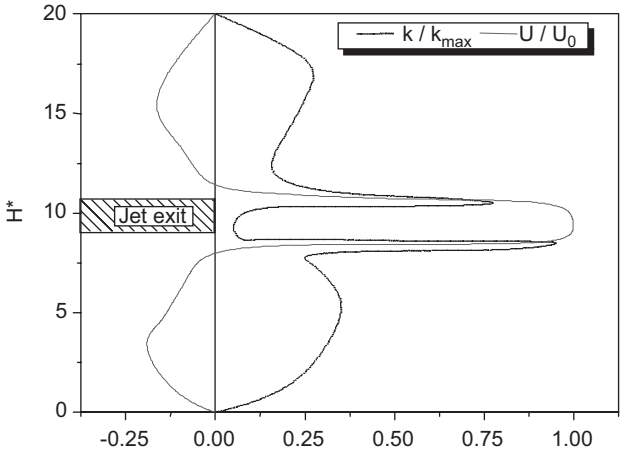

Fig. 5. Jet exit conditions (experiment): dimensionless mean velocity and kinetic energy, $x/e = 2$, Re = 4000, $H_0^* = 20$, $L_0^* = 100$.

All dimensionless geometrical quantities will be defined using the previous parameters U_0 and e in order to easily generalise the results to other jet–cavity interactions.

5.2. The jet exit conditions

The plane duct produces a fully turbulent plane jet with a low turbulence rate at the exit. Fig. 5 shows the measured normalized velocity (U/U_0) and the kinetic energy profiles (k/k_{max}), k_{max} being the maximum kinetic energy in the jet exit section.

5.3. Effect of the cavity aspect ratio on the unsteady regime

5.3.1. Effect of the wall bottom: influence of the cavity length

In order to study the effect of the cavity length, several calculations were carried out for higher values of L_0^* compared to the reference value $L_0^* = 50$ considered in Mataoui et al. (2001). The dimensionless time-averaged velocity modulus $(U^2+V^2)^{1/2}/U_0$ and streamlines are reported in Fig. 6 for three cases ($L_0^* = 50$, $L_0^* = 100$ and $L_0^* = 150$) at every quarter of a time period. For elongated cavities ($L_0^* > 50$), it appears that the fluid is almost quiescent in the bottom region.

The flow pattern is very similar to the one obtained in the original case ($L_0^* = 50$) except for a longitudinal transfer induced by the inactive flow pad in the bottom.

Experimentally, the visualisation of the flow interaction confirms the numerical predictions. Fig. 7 shows four photograph shots within one time period of the oscillation for two aspect ratios ($L_0^* = 50$ and $L_0^* = 100$). It appears that the distance of the jet impingement on the lateral walls is practically very similar to the corresponding values calculated for the cavities $L_0^* = 50$ and $L_0^* = 100$ at each quarter of period. In the bottom region, the white smoke is blocked and the flow is practically motionless in the case of an elongated cavity ($L_0^* = 100$).

The dimensionless pressure, kinetic energy and the shape parameter ($P/\rho U_0^2$, k/U_0^2 and ξ) contours for $L_0^* = 50$ and $L_0^* = 100$ are, respectively, reproduced in Figs. 8–10. The analysis of these diagrams highlights the deviation of the jet towards one of the two lateral walls coupled with a weak activity in the bottom region of the cavity for $L_0^* = 100$. This is

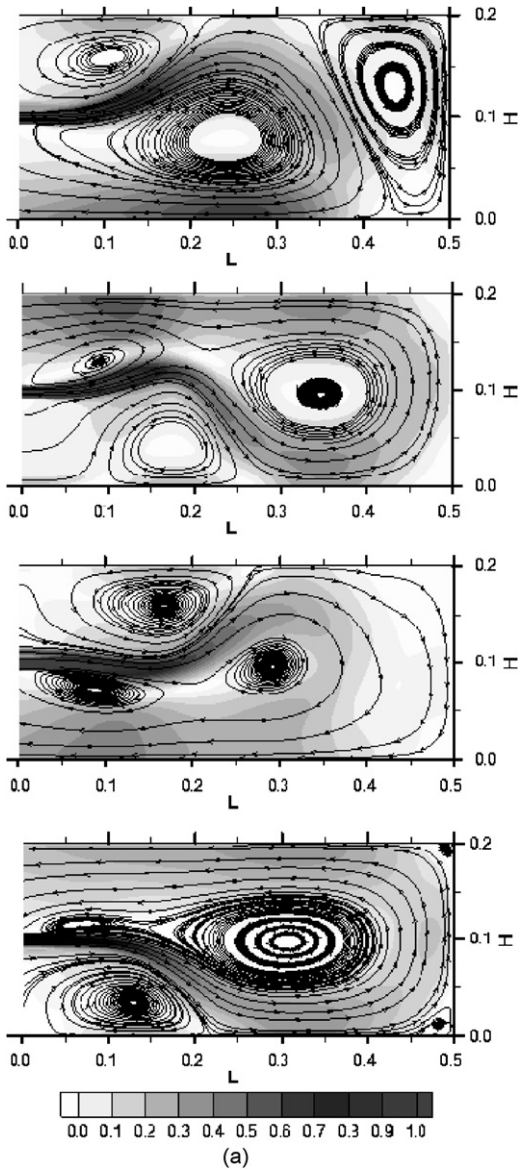

Fig. 6. (a) Dimensionless time-averaged velocity magnitude $(U^2+V^2)^{1/2}/U_0$ and streamlines at $T/4$, $T/2$, $3T/4$ and T. $H_0^* = 20$, $L_0^* = 50$, Re = 4000; axes units in m. (b) Dimensionless time-averaged velocity magnitude $(U^2+V^2)^{1/2}/U_0$ and streamlines at $T/4$, $T/2$, $3T/4$ and T. $H_0^* = 20$, $L_0^* = 100$, Re = 4000; axes units in m. (c) Dimensionless time-averaged velocity magnitude $(U^2+V^2)^{1/2}/U_0$ and streamlines at $T/4$, $T/2$, $3T/4$ and T. $H_0^* = 20$, $L_0^* = 150$, Re = 4000; axes units in m.

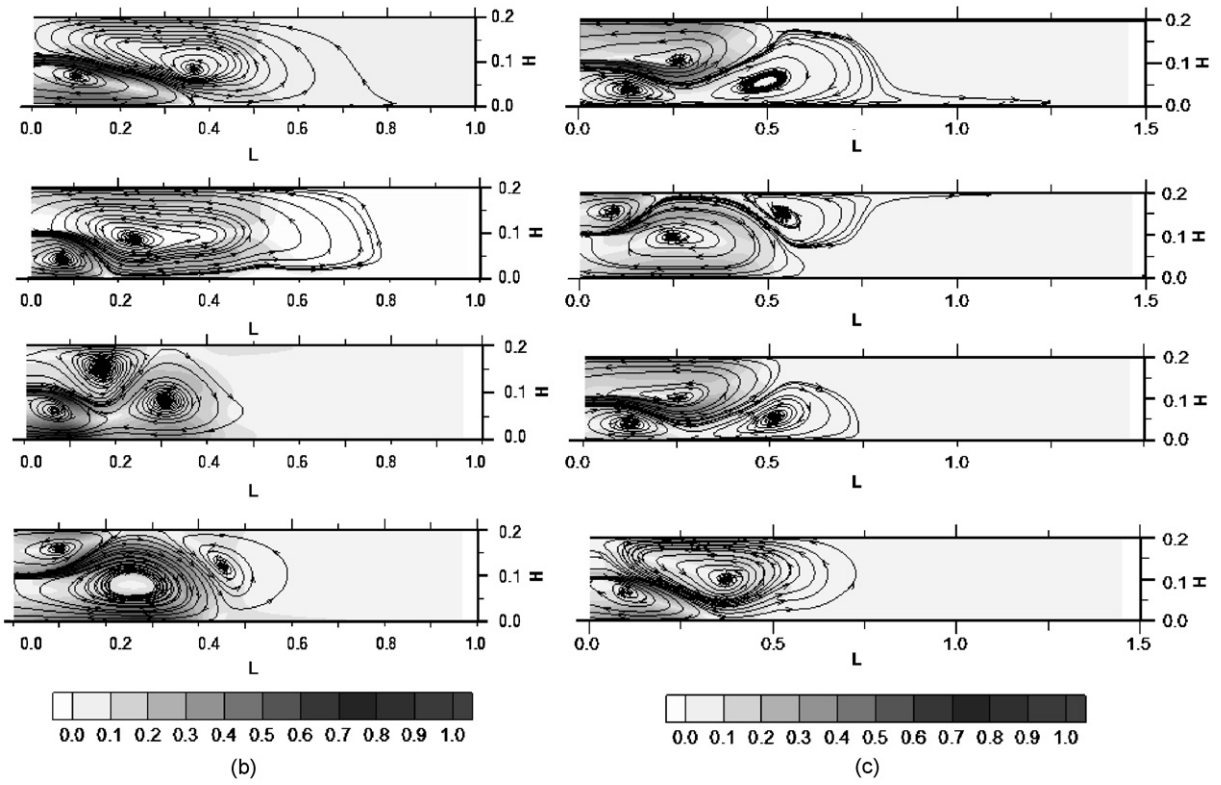

Fig. 6. (*Continued*)

a proof that the jet deviations are mainly due to the existence of horizontal side-walls, creating low pressure regions which are the cause of the mechanism of self-sustained oscillations.

In the case of elongated cavities, the bottom wall distance does not have a significant effect on the oscillation mechanism. The jet lateral impingement is almost the same for all the elongated cavities.

5.3.2. *Effect of the lateral walls: influence of the cavity height*

We only consider here the symmetrical interaction case with the jet located at the transverse mid-plane of the cavity. Calculations made with twice the value of the cavity height are illustrated in Fig. 11, showing dimensionless time-averaged velocity modulus $(U^2+V^2)^{1/2}/U_0$ and velocity vector plots. In this geometry, the flow regime switched to a non-oscillatory state. So, when the cavity height is increased the oscillations disappear and the flow becomes steady in the mean. The jet impinges the bottom wall of the cavity perpendicularly, producing a frontal interaction. The impingement mechanism is illustrated by the pressure, kinetic energy and the shape parameter contours, respectively, reported in Figs. 12–14. In general, if the cavity height is larger compared to the distance of impingement, the lateral interaction disappears, because the pressure sink due to the Coanda effect is too weak to cause a deflection of the jet (Bernard et al., 2000).

It is also worth mentioning that many past studies have shown that the oscillations occur also in the case of symmetrical interaction with an open cavity at the downstream end (open cavity at either ends) (Maurel, 1994; Maurel et al., 1996; Villermaux and Hopfinger, 1994; Uzol and Camci, 2002; Lawson and Davidson, 1999; Gevici et al., 2003).

5.3.3. *Flow regime map*

In order to check the effect of the cavity geometrical characteristics on the jet–cavity interaction phenomenon, several symmetrical configurations were considered both numerically and experimentally. In these tests, the width of the cavity and the jet nozzle exit thickness were kept constant. In the experimental approach, it was only possible to vary the longitudinal distance L_0 of the jet exit to the bottom wall by means of more elongated cavities. In the numerical approach, a large amount of tests were considered through the variation of both the longitudinal distance L_0 (17 values

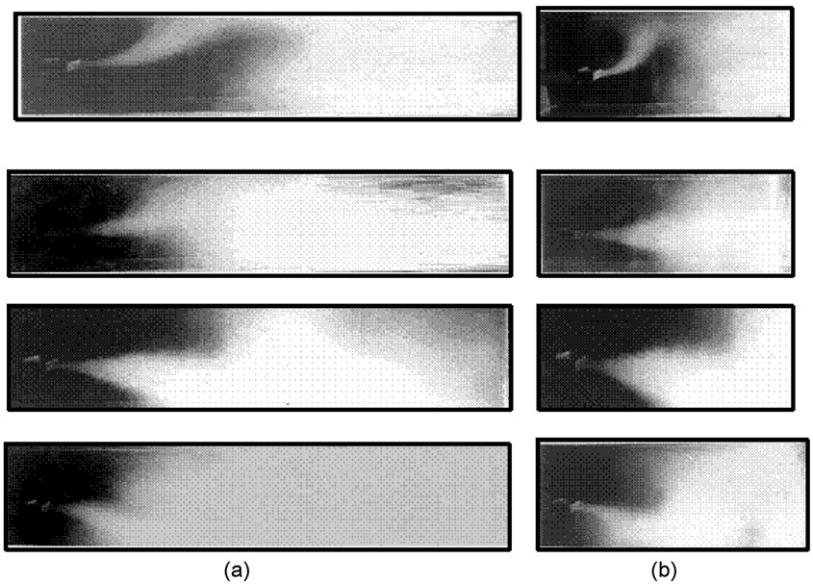

Fig. 7. Flow visualisation, $H_0^* = 20$, Re = 4000: (a) $L_0^* = 100$ and (b) $L_0^* = 50$.

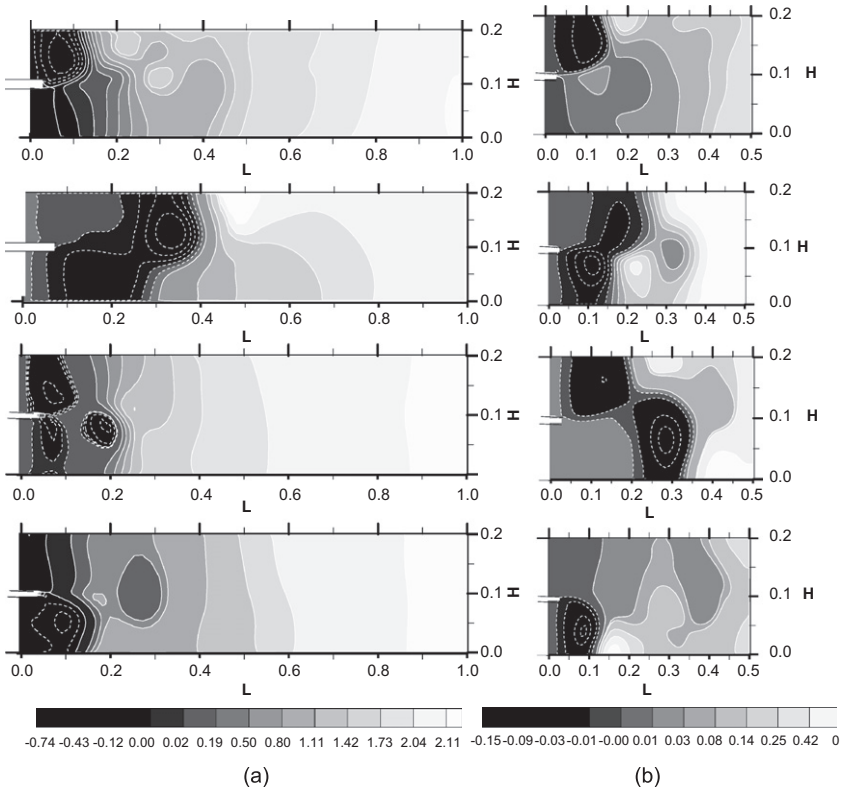

Fig. 8. Calculated instantaneous dimensionless pressure contours within one period of time, $H_0^* = 20$, Re = 4000; axes units in m: (a) $L_0^* = 100$ and (b) $L_0^* = 50$.

of L_0^* ranging from 25 to 400) and the cavity height H_0 (4 values of H_0^* ranging from 20 to 50). The type of regime is determined experimentally or numerically in the same way, using a time analysis of the instantaneous velocity signal at several station points inside the cavity and then confirmed by visualisation. We have thus detected three types of flow

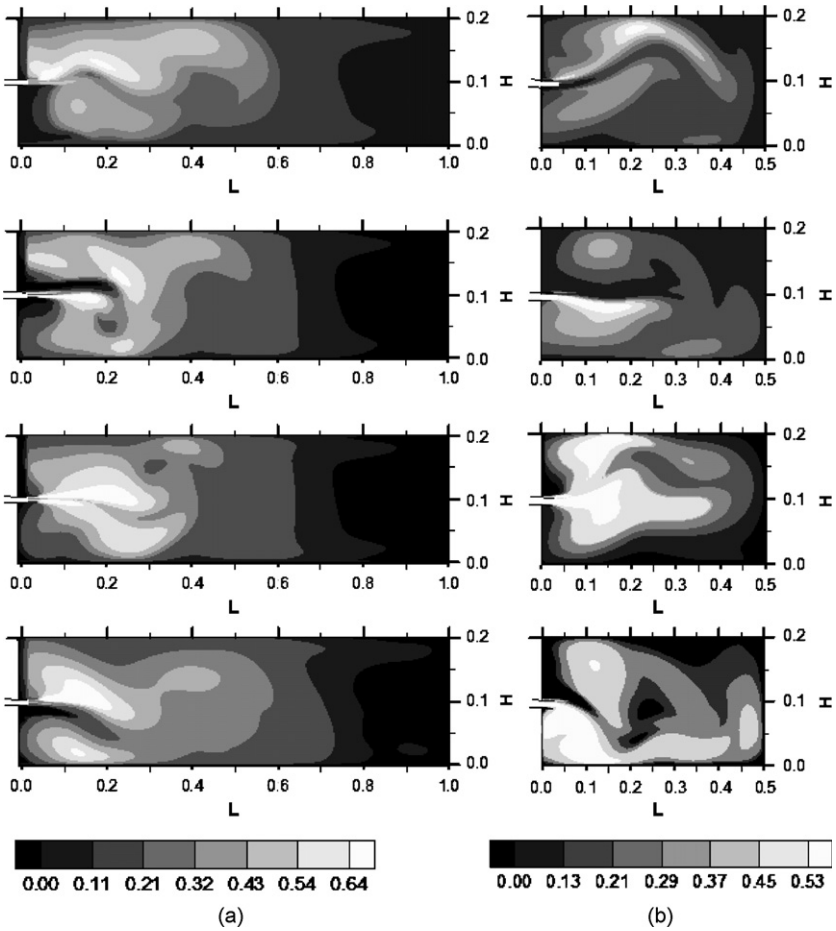

Fig. 9. Calculated instantaneous dimensionless kinetic energy contours within one period of time, $H_0^* = 20$, Re = 4000; axes units in m: (a) $L_0^* = 100$ and (b) $L_0^* = 50$.

regime depending on the cavity height and length. The flow would switch from one regime to another depending on the geometrical parameters. In the no-oscillation regime, the flow is steady, and in the stable oscillation regime the unsteadiness corresponds to a periodic behaviour, whilst in the intermediate unstable oscillation case, the unsteadiness corresponds to a more complex behaviour with several frequencies and apparently irregular oscillations. These three distinct zones are delimited on the flow regime map in Fig. 15: no oscillation, unstable oscillation and stable oscillation zones are separated by transition curves. This diagram was established and checked for Reynolds numbers ranging from 1000 to 10 000 and numerical results are in agreement with the corresponding experimental findings. A similar diagram was experimentally obtained by Shakouchi (1981) and Lawson et al. (2005).

For $L_0^* > 150$, the transition curve between the unstable oscillation and the stable oscillation zones can be fairly well approximated by a linear curve (Fig. 15):

$$L_0^* = 9.85H_0^* - 193.28.$$

5.4. Time analysis of the oscillatory flow

The jet oscillations were experimentally and numerically analysed through the time evolution of the instantaneous velocity signals at predetermined station points inside the cavity. The numerical prediction proved to be similar to the experimental behaviour (Fig. 16). An example of stick spectrum of the measured velocity signal is given in Fig. 17 for a

periodic case, it clearly shows the peaks corresponding to the periodic mean oscillation (fundamental mode and harmonics) that are superposed to the background true turbulent field. For all the oscillatory cases considered within the limits of the stable oscillation regime given in Fig. 15, the calculated frequency of the jet flapping inside the cavity varies linearly versus the Reynolds number (Fig. 18). The unstable oscillation regime illustrated in Fig. 16(g) and delineated in Fig. 15 does not show a dominant frequency. The behaviour is more complex and its study was not detailed further.

When the impingement distance is less than a certain critical value, the cavity bottom does not have any appreciable effect on the oscillation frequency. In order to examine the effect of the vertical and longitudinal cavity sizes on the oscillatory phenomena, we have determined the oscillation frequency as a function of the geometrical characteristics of the cavity. Regarding the effect of the bottom wall, the oscillation phenomenon practically remains identical with an almost constant frequency (Fig. 18) with the increase of the cavity length. However, if the height of the cavity increases, the oscillation frequency slightly decreases (Fig. 19). Fig. 19 is in good agreement with several previous studies (Shakouchi, 1981; Shakouchi et al., 1982; Lawson et al., 2005), and confirms the assumption that the oscillations are mainly produced by the lateral cavity walls.

The Strouhal number is found to be independent from Reynolds numbers (at large Reynolds numbers) *i.e.*, $St = f(Re) = \text{constant}$. Such results are practically in good agreement with all research works on oscillatory jet–cavity interaction for similar configurations which were previously mentioned. Additionally, the analysis deduced from Fig. 20, shows an important phase shift between the mean pressure and the velocities components. The pressure phase is ahead from the phase of the other mean and turbulent quantities. These phase shifts confirm the existence of a feedback mechanism and time lag effects (Ayukawa and Shakouchi, 1976). Hence, the observed phase shift appears to be linked to the pressure response which accompanies the deviation of the jet during the oscillatory motion.

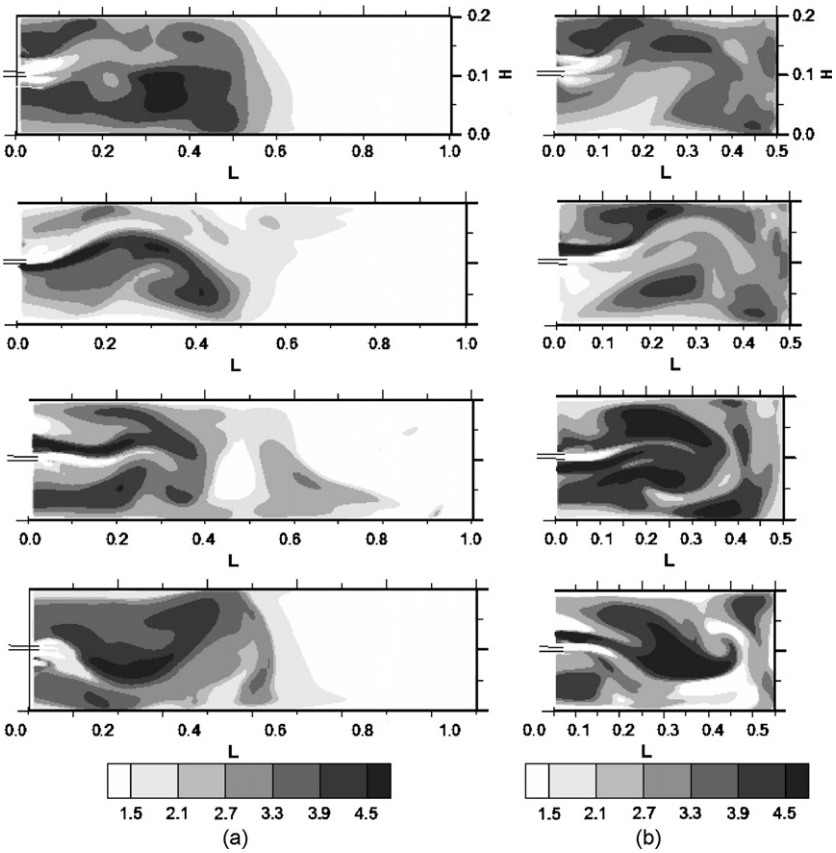

Fig. 10. Calculated instantaneous shape parameters ($\xi = k_P/k_T$) contours within one period of time, $H_0^* = 20$, Re = 4000; axes units in m: (a) $L_0^* = 100$ and (b) $L_0^* = 50$.

5.5. Mechanisms of oscillation

The self-sustained jet oscillations inside the cavity are governed by the action of the pressure variations within the two laterals eddies developing at both sides of the jet axis. A better description of the mechanism emerges from Fig. 21. The instantaneous flow rates Q_{upper} and Q_{lower}, respectively through the upper and the lower open boundaries, are expressed as functions of the instantaneous difference between the corresponding pressures at these boundaries ($\Delta P = P_{lower} - P_{upper}$). At the inlet, the considered flow rate Q_0 originating from the jet is assumed constant. The arrows in the diagrams of Fig. 21 indicate the circulation direction within one period of oscillation. When the upper side eddy is flowing out, the pressure difference ΔP increases whilst the upper flow rate Q_{upper} increases and the lower flow rate Q_{lower} decreases, with the jet reaching its most deflected position. Then, the pressure difference ΔP decreases simultaneously to an increase of Q_{upper} and a decrease of Q_{lower}, while the upper exit is blocked by the lateral eddy and the jet deflection is reversed. Therefore, the phenomenon is symmetrically repeated.

All the configurations that were considered in this study are symmetrical, and the corresponding diagrams are symmetrical about the mid-plane position too. In this central position of the jet, the difference between the corresponding pressures at the exit sections ($\Delta P = P_{lower} - P_{upper}$) is negligible ($\Delta P = 0$) and the outflow is split into two

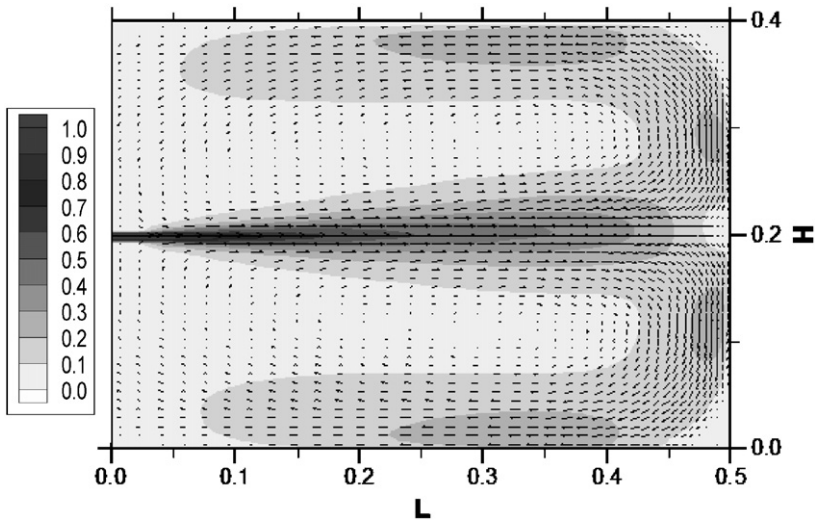

Fig. 11. Dimensionless time-averaged velocity magnitude $(U_2 + V_2)^{1/2}/U_0$ levels and vector plot, $L_0^* = 50$, $H_0^* = 40$, Re = 4000; axes units in m.

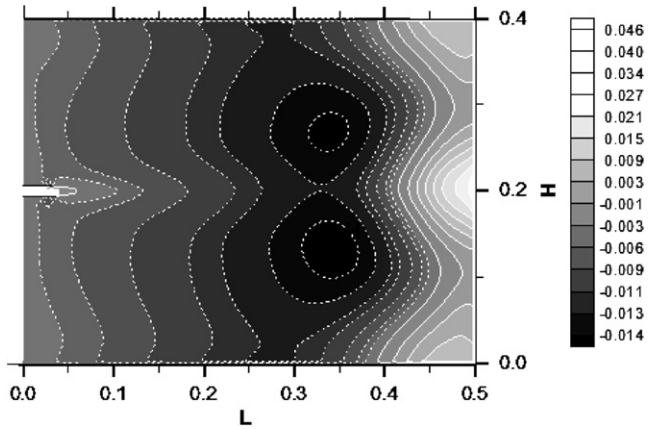

Fig. 12. Dimensionless pressure levels $(P/\rho U_0^2)$, $L_0^* = 50$, $H_0^* = 40$, Re = 4000; axes units in m.

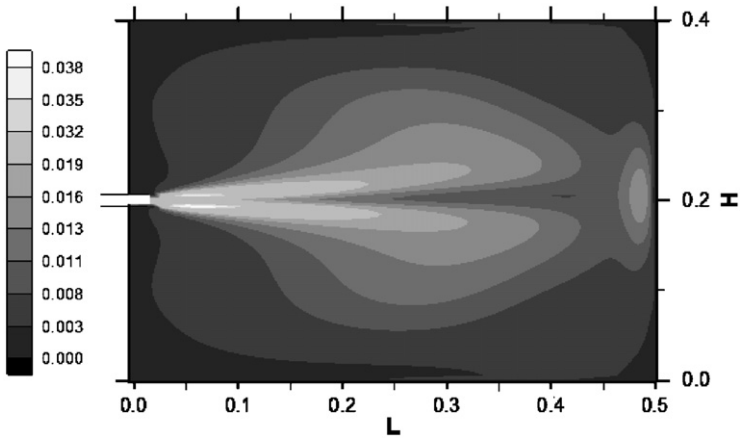

Fig. 13. Dimensionless kinetic energy levels (k/U_0^2), $L_0^* = 50$, $H_0^* = 40$, Re = 4000; axes units in m.

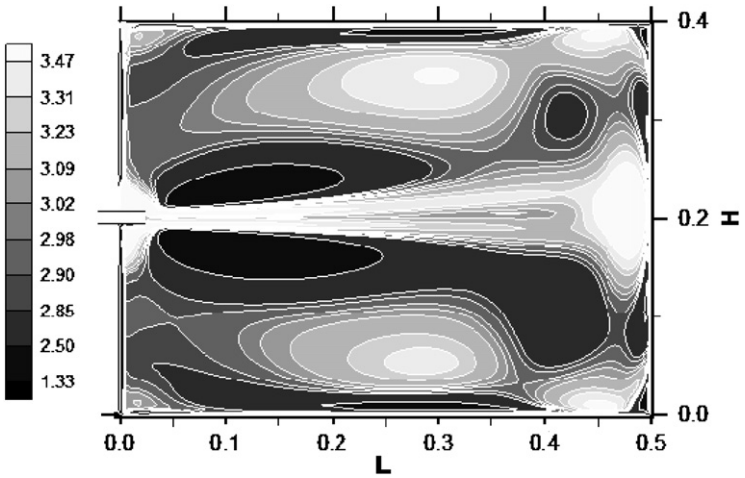

Fig. 14. Shape parameter levels ($\xi = k_P/k_T$), $L_0^* = 50$, $H_0^* = 40$, Re = 4000; axes units in m.

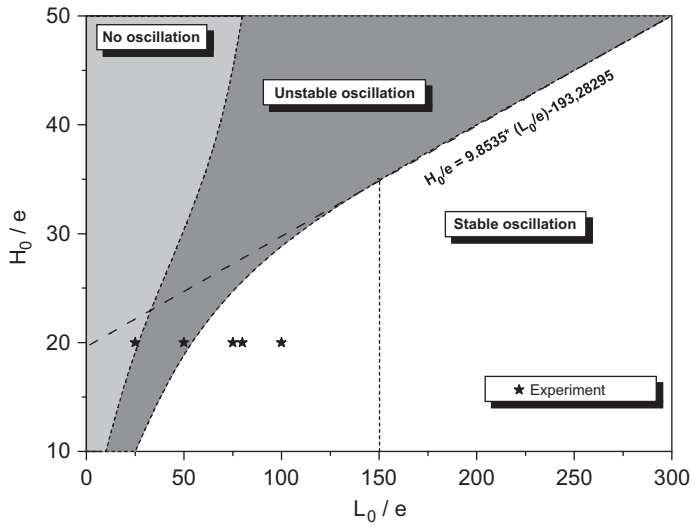

Fig. 15. Flow regime map for fixed width of cavity (0.2 m) and thickness of the jet ($e = 0.01$ m), Re range from 1000 to 10 000.

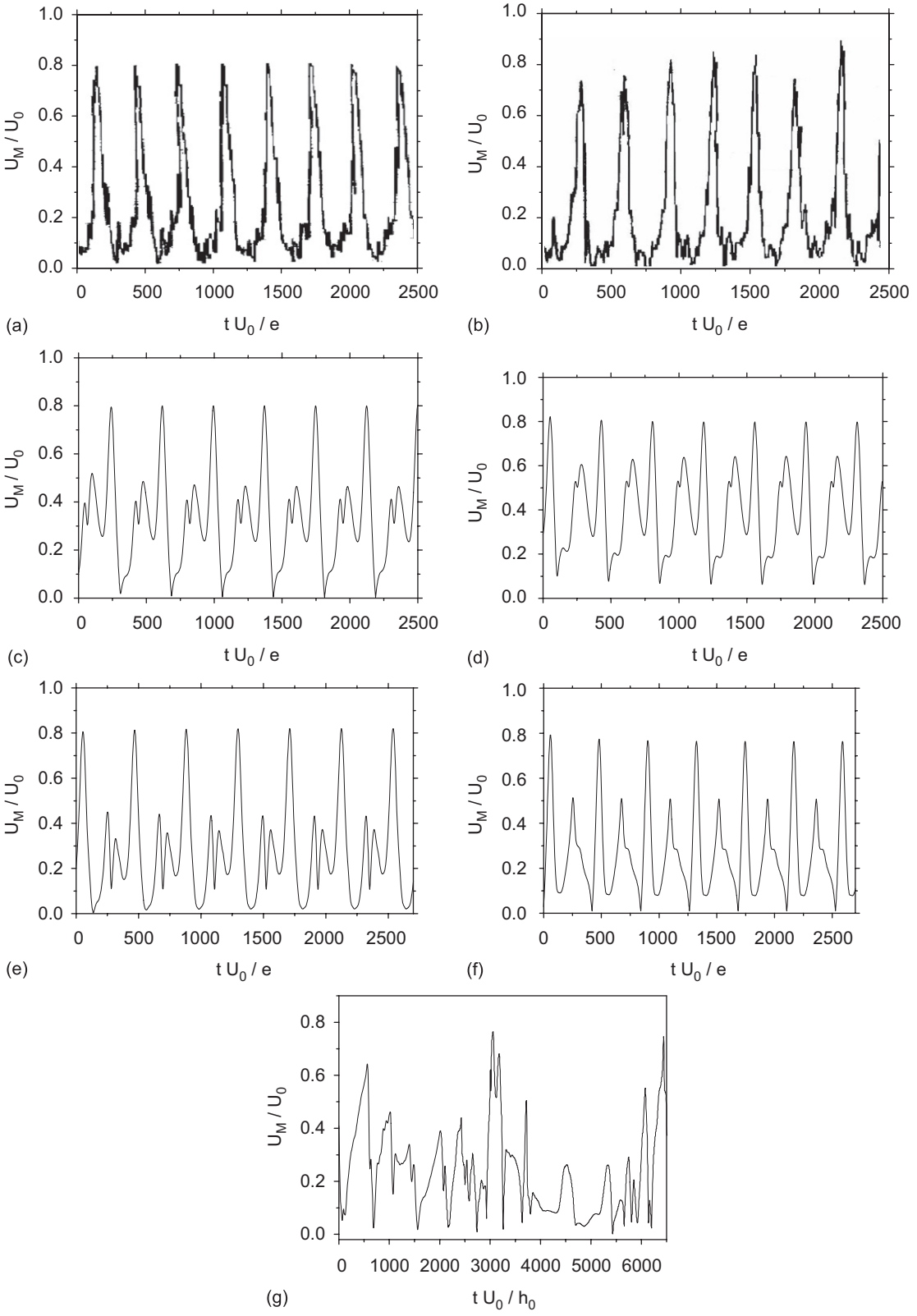

Fig. 16. Time evolution of velocity signal, $H_0^* = 20$, $\mathrm{Re} = 4000$, $x_M/e = 10$, $h_M/e = 10$. Experiment: (a) $L_0^* = 50$ and (b) $L_0^* = 100$. Computation: (c) $L_0^* = 50$, (d) $L_0^* = 100$, (e) $L_0^* = 150$, (f) $L_0^* = 200$ and (g) $L_0^* = 30$, example of unstable unsteady behaviour.

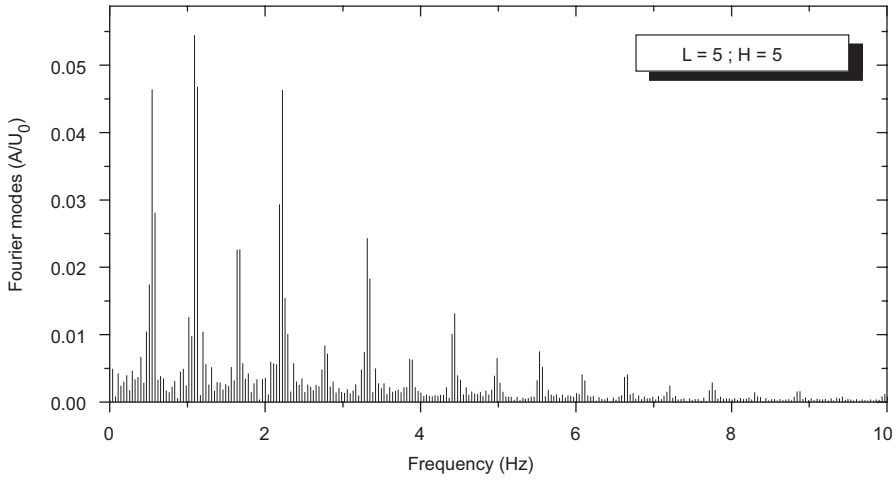

Fig. 17. Example of stick spectrum of the measured velocity signal, $L_0/e = 100$, $H_0/e = 20$; L and H given in cm.

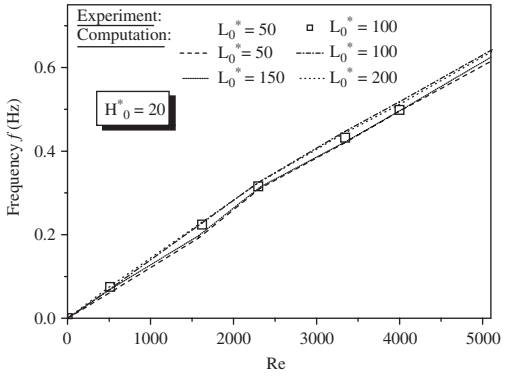

Fig. 18. Variation of frequency as a function of the Reynolds number. Influence of impingement distance ($H_0^* = 20$).

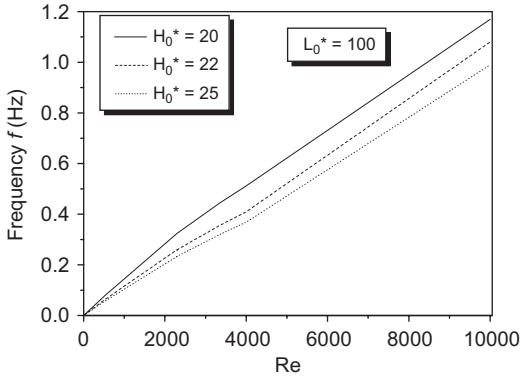

Fig. 19. Variation of the frequency versus the Reynolds number. Influence of impingement distance ($L_0^* = 100$).

equal parts ($Q_{\text{upper}} = Q_{\text{lower}} = -0.5Q_0$). For the other locations of the jet, Q_{lower} becomes maximum when the corresponding Q_{upper} becomes minimum and *vice versa*. In all cases, the conservation of the total flow rate implies $Q_{\text{upper}} + Q_{\text{lower}} = -Q_0$. A similar behaviour was also experimentally verified by Shakouchi (1981).

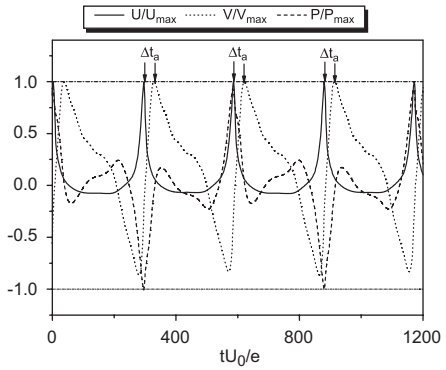

Fig. 20. Time evolution of U, V and P: phase shift between velocity components and pressure Δt_a ($L_0^* = 100$, $H_0^* = 20$, $x_M/e = 15$, $h_M/e = 10$, Re = 4000).

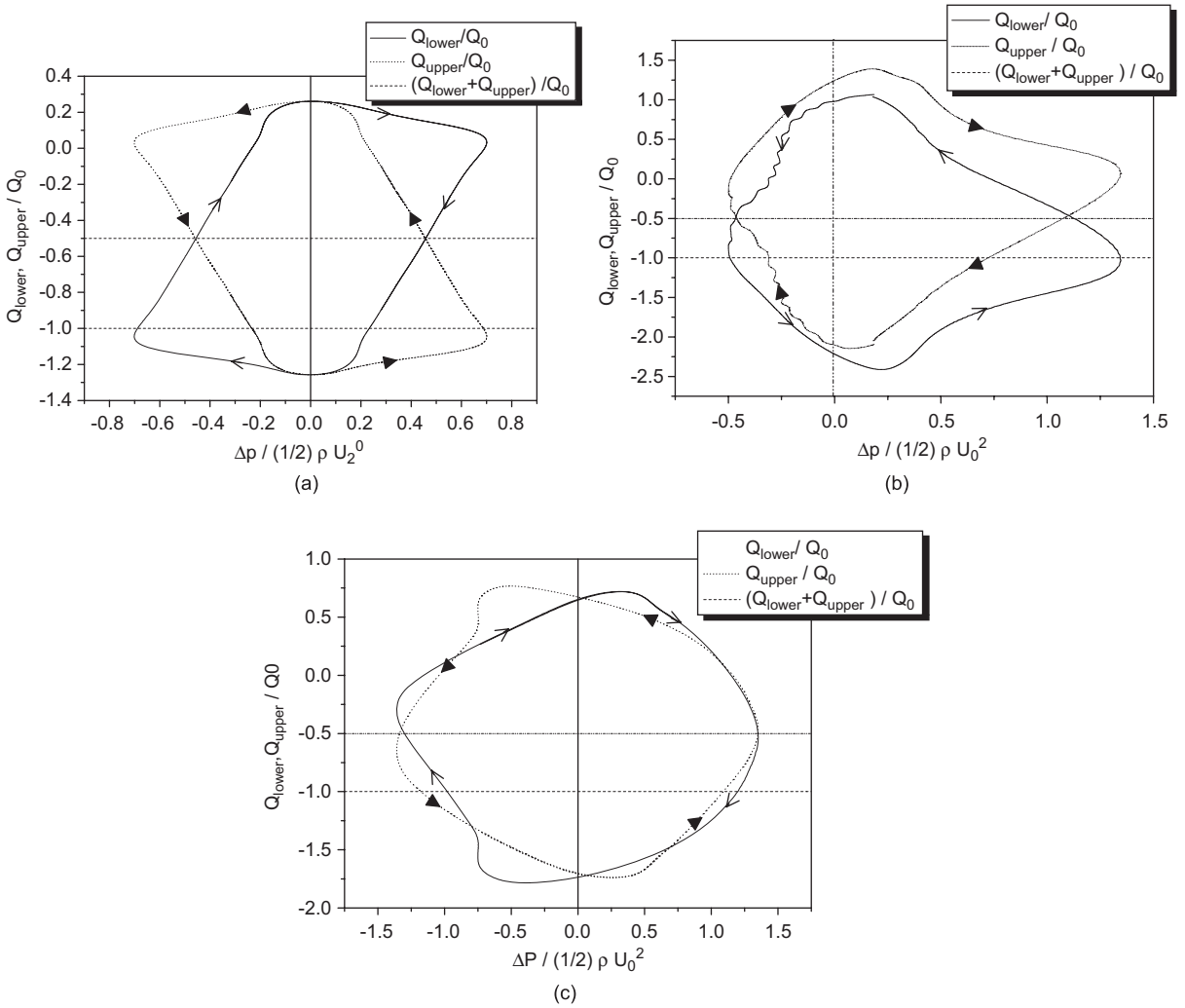

Fig. 21. Dynamic cycles: calculated flow rate as a function of the mean pressure: (a) $H_0^* = 20$, $L_0^* = 50$; (b) $H_0^* = 20$, $L_0^* = 100$ and (c) $H_0^* = 20$; $L_0^* = 200$.

6. Conclusion

The interaction of a turbulent plane jet inside a rectangular cavity generates complex flow behaviour that can be efficiently predicted using the URANS approach. The present study combines numerical and experimental approaches including measurements and flow visualisation. A good agreement was achieved between these approaches.

In this study case, we were mainly interested in the effect of the geometrical parameters of the cavity, particularly its aspect ratio (height H_0 to length L_0).

Several flow regimes were observed depending on the geometrical parameters:

(i) the stable oscillation flow (periodic oscillations);
(ii) the non-oscillatory regime (steady flow);
(iii) the unstable oscillations case (intermediate case with irregular oscillations).

These results were synthesized in a diagram which delimits the different flow regimes and it emerged that they are practically independent of the Reynolds number (provided the Reynolds number is sufficiently high).

In the case of the steady mode which occurred for large values of H_0/L_0, a symmetrical frontal interaction was obtained (with a perpendicular impingement of the jet on the bottom wall of the cavity).

For the oscillatory flow, the fundamental frequency of the oscillations was obtained for several geometrical and dynamical parameters. The jet flapping frequency increases linearly with the Reynolds number and decreases moderately with the height of the cavity. Additionally, one must emphasize the occurrence of a phase shift between the pressure and the velocity components, kinetic energy and dissipation. It is remarkable how URANS one-point turbulence closure succeeds in capturing the oscillatory behaviour of the flow without any specific empirical modification (Bosch and Rodi, 1996; Kato and Launder, 1993).

The jet oscillation mechanism is related to the pressure effects as shown on the diagrams (Q_{upper} and Q_{lower} versus ΔP). Particularly, the periodic motion of the two eddies which periodically inflate and deflate on both sides of the jet axis, is in complete agreement with the conclusions of previous studies (Mataoui et al., 2001, 2003).

The present study also allowed a detailed description of the flow instantaneous structure. Given the fact that the driving phenomenon of the confined jet oscillations closely relates to pressure effects, it enabled us to use a simplified model within the wall layer by means of wall functions. However, this approach would not be suitable for a fine description of the near-wall region, particularly the impact areas.

References

Ayukawa, K., Shakouchi, T., 1976. Analysis of a jet attaching to an offset parallel plate (oscillation of a jet). Bulletin of JSME 19 (130), 395–401.

Battaglia, F., Kulkarni, A.K., Feng, J., Merkle, C.L., 1998. Simulations of planar flapping jets in confined channels. AIAA Journal 36 (8), 1425–1431.

Bernard, A., Brizzi, L.-E., Bousgarbies, J.-L., 2000. A comparison of flow visualisation and wall pressure measurements for a jet impinging on a plane surface. Experiments in Fluids 29, 23–29.

Bosch, G., Rodi, W., 1996. Simulation of vortex shedding past a square cylinder near a wall. International Journal of Heat and Fluid Flow 17, 267–275.

Bourque, C., Newman, B.G., 1960. Reattachment of a two dimensional incompressible jet to an adjacent flat plate. Aeronautical Quarterly XI, 201–232.

Bruun, H.H., 1995. Hot-Wire Anemometry, Principles and Signal Analysis. Oxford University Press, Oxford.

Cooper, D., Jackson, D.C., Launder, B.E., Liao, G.X., 1993. Impinging jet studies for turbulence model assessment—I. Flow field experiments. International Journal of Heat and Mass Transfer 36 (10), 2675–2684.

Craft, T.J., Graham, L.J.W., Launder, B.E., 1993. Impinging jet studies for turbulence model assessment—II. An examination of the performance of four turbulence models. International Journal of Heat and Mass Transfer 36 (10), 2685–2697.

Denisikhina, D.M., Bassina, I.A., Nikulin, D.A., Strelets, M.Kh., 2005. Numerical simulation of self-excited oscillation of a turbulent jet flowing into a rectangular cavity. High Temperature 43 (4), 568–579.

Gebert, B.M., Davidson, M.R., Rudman, M.J., 1998. Computed oscillations of a confined submerged liquid jet. Applied Mathematics Modelling 22, 843–850.

Gevici, M., Oshkai, P., Rockwell, D., Lin, J.-C., Pollack, M., 2003. Imaging of the self excited oscillation of flow past a cavity during generation of a flow tone. Journal of Fluids and Structures 18, 665–694.

Gloerfelt, X., Lafon, P., 2005. Direct computation of the noise induced by a turbulent flow through a diagram in a duct at low Mach number. Euromech Colloquium 467: Turbulent Flow and Noise Generation, July 18–20, Marseille, France.

Guo, B., Langrish, A.G., Fletcher, D.F., 2001. An assessment of turbulence models applied to the simulation of a two-dimensional submerged jet. Applied Mathematics Modelling 25, 635–653.

Hanjalic, K., Launder, B.E., Schiestel, R., 1980. Multiple time-scale concepts in turbulent transport modelling. In: Bradbury, L.S., Durst, F., Launder, B.E., Schmidt, F.W., Whitelaw, J.H. (Eds.), Turbulent Shear Flows 2, Selected papers from the 2nd International Symposium on Turbulent Shear Flows. Springer, pp. 36–49.

Hebrard, P., Liousse, F., Calvet, P., 1979. Méthodes et moyens de mesure de débit de gaz, Collection des monographies du Bureau National de Métrologie. Editions Chiron, Paris.

Kato, M., Launder, B.E., 1993. The modelling of turbulent flow around a stationary and vibrating square cylinder. In: Proceedings of the 9th Symposium on Turbulent Shear Flows, Kyoto, vol. 9, pp. 10.4.1.

Kolšek, T., Jelić, N., Duhovnik, J., 2007. Numerical study of flow asymmetry and self-sustained jet oscillations in geometrically symmetric cavities. Applied Mathematical Modelling 31 (10), 2355–2373.

Launder, B.E., Schiestel, R., 1978. Sur l'utilisation d'échelles temporelles multiples en modélisation des écoulements turbulents. C.R. Académie des Sciences Sér. A, vol. 286, pp. 709–712.

Launder, B.E., Spalding, D.B., 1974. The numerical computation of turbulent flows. Computer Methods in Applied Mechanics and Energy 3, 269–289.

Lawson, N.J., 2001. Self-sustained oscillation of a submerged jet in a thin rectangular cavity. Journal of Fluid and Structures 15, 59–81.

Lawson, N.J., Davidson, M.R., 1999. Cross flow characteristics of an oscillating jet in a thin slab casting mould. Transactions of the ASME 121, 588–595.

Lawson, N.J., Arrunda, M.P., Davidson, M.R., 2005. Control of a submerged jet in a thin rectangular cavity. Journal of Fluids and Structures 20 (8), 1025–1042.

Mataoui, A., Schiestel, R., Salem, A., 2001. Flow regimes of interaction of a turbulent plane jet into a rectangular cavity. Experimental approach and numerical modelling. Journal of Flow, Turbulence and Combustion 67 (4), 267–304.

Mataoui, A., Schiestel, R., Salem, A., 2003. Study of the oscillatory regime of a turbulent plane jet impinging in a rectangular cavity. Applied Mathematical Modelling 27 (2), 89–114.

Maurel, A., 1994. Instabilité d'un jet confiné, Thèse de Doctorat de l'Université Paris VI.

Maurel, A., Ern, P., Zielinska, B.J.A., Wesfreid, J.E., 1996. Experimental study of self-sustained oscillations in a confined jet. Physical Review E 54, 3643–3651.

Molloy, N.A., 1969. Oscillatory flow of a jet into a blind cavity. Nature 224, 1192–1194.

Ogab, A., 1985. Contribution à l'étude de l'évolution d'un jet plan turbulent dans une cavité de section rectangulaire. Thèse de Magister, Mécanique des Fluides, USTHB Alger.

Pacheu, T., Le Guer, Y., Lalanne, L., Creff, R., 2000. Étude expérimentale des auto-oscillations d'un jet plan confiné au sein d'une cavité contenant un obstacle. C. R. Académie des Sciences Paris, Mécanique des Fluides/Fluid Mechanics, 328, Sér II b, pp. 297–303.

Patankar, S.V., 1980. Numerical Heat Transfer and Fluid Flow. Hemisphere Publishing Corp. & McGraw-Hill.

Pereira, J.C., Sousa, J.M.M., 1995. Experimental and numerical investigation of flow oscillations in a rectangular cavity. ASME Journal of Fluids Engineering 117, 68–74.

Rockwell, D., Naudascher, E., 1979. Self-sustained oscillations of impinging free shear layers. Annual Review of Fluid Mechanics 11, 67–94.

Sarohia, V., 1977. Experimental investigation of oscillations in flows over shallow cavities. AIAA Journal 15 (7), 984–991.

Schiestel, R., 1983. Sur le concept d'échelles multiples en modélisation des écoulements turbulents. Journal de Mécanique Théorique et Appliquée, Part I, 2 (3), 417–Part II, 2 (4), 601.

Schiestel, R., 1987. Multiple-time-scale modelling of turbulent flows in one point closures. Physics of Fluids 30 (3), 722–731.

Schiestel, R., 2006. Méthodes de modélisation et de Simulation des Ecoulements Turbulents. Hermès/Lavoisier, Paris.

Shakouchi, T., 1981. An experimental study on the cavity type fluidic oscillator. Research Reports of the Faculty of Engineering, Mie University, Japan, No. 6, December, pp. 1–13.

Shakouchi, T., 1989. A New fluidic oscillator, flow-meter, without control port and feedback loop. Journal of Dynamic Systems, Measurement and Control 111, 535–539.

Shakouchi, T., Kuzuhara, S., 1982. Analysis of a jet attaching to an offset parallel plate (influence of an opposite wall). Bulletin of JSME 25 (203), 766–773.

Shakouchi, T., Suematsu, Y., Ito, T., 1982. A study on oscillatory jet in a cavity. Bulletin of JSME 25 (206), 1258–1265.

Sinha, S.N., Gupta, A.K., Oberai, M.M., 1982. Laminar separating flow over backsteps and cavities. Part II: Cavities. AIAA Journal 20 (3), 370–375.

Uzol, O., Camci, C., 2002. Experimental and computational visualisation and frequency measurements of the jet oscillation inside a fluidic oscillator. Journal of Visualisation 4, 88–96.

Villermaux, E., Hopfinger, E.J., 1994. Self-sustained oscillations of a confined jet: a case study for the non-linear delayed saturation model. Physica D 72, 230–243.

Yap, C.R., 1987. Turbulent heat and momentum transfer in recirculating and impinging flows. University of Manchester Institute of Science and Technology, Ph.D. Thesis, Victoria University of Manchester, and UMIST Report TFD/87/1.